Measurement and analysis of thermal photoemission from a dispenser cathode

Kevin L. Jensen
Code 6841, ESTD, Naval Research Laboratory, Washington, D.C. 20375, USA

Donald W. Feldman, Matt Virgo, and Patrick G. O'Shea*
Institute for Research in Electronics & Applied Physics, University of Maryland, College Park, Maryland 20742, USA
(Received 30 May 2003; published 5 August 2003)

Photocathodes for free electron lasers (FELs) are required to produce nano-Coulomb pulses in picosecond time scales with demonstrable reliability, lifetime, and efficiency. Dispenser cathodes, traditionally a rugged and long-lived thermionic source, are under investigation to determine their utility as a photocathode and have shown promise. The present study describes theoretical models under development to analyze experimental data from dispenser cathodes and to create predictive time-dependent models to predict their performance as an FEL source. Here, a steady-state model of a dispenser cathode with partial coverage of a low work function coating and surface nonuniformity is developed. Quantitative agreement is found for experimental data, especially with regard to temperature, field, laser intensity, and quantum efficiency versus laser wavelength dependence. In particular, for long wavelength incident lasers of sufficient intensity, the majority of the absorbed energy heats the electron gas and background lattice, and photoemission from the heated electron distribution constitutes the emitted current.

DOI: 10.1103/PhysRevSTAB.6.083501 PACS numbers: 85.60.Ha, 79.40.+z, 79.60.–i, 52.59.–f

I. INTRODUCTION

Photoemission sources for free electron lasers [1] under development for a variety of scientific and industrial applications face unprecedented operational demands. Free electron lasers (FELs) need photocathodes to be long lived, reliable, capable of producing nano-Coulomb electron bunches in picosecond time scales, and illuminated by drive lasers using the longest wavelength permissible (preferably 532 nm or longer). Such requirements are often conflicting. Low work function coatings on semiconductor photocathodes, produced by empirical techniques, have excellent quantum efficiency (QE), but suffer and degrade prematurely under vacuums characteristic of rf photoinjector guns and generally have response times [2,3] that are too great. Metal photocathodes are rugged, long lived, and prompt emitters, but they generally have low QE and require ultraviolet (UV) drive lasers at 266 nm [4,5]. The wavelength of a drive laser is obtained by nonlinear conversion crystals which reduce a 1064 nm laser by doubled (512 nm), tripled (355 nm), or quadrupled (266 nm) Nd:YAG conversion, with conversion efficiencies of approximately 50%, 30%, or 10%, respectively. For the UV case, therefore, a great deal of waste heat will be dumped into the crystals, altering their operation and leading to nonlinear performance. Moreover, the nonlinear conversion process introduces fluctuations that scale as (laser intensity)^n, where n is the harmonic number (4 for 266 nm), and such fluctuations appear in the resulting electron pulses, resulting in a degraded FEL operation. Regardless, photocathodes remain the only viable option for high power FELs: while thermionic sources have been used in the past for FELs, they cannot be switched on the picosecond time scale, and the resultant emittance of the electron beam is too large to allow for lasing at desired wavelengths.

The thermal dispenser cathode has recently been proposed and investigated as a potential photocathode candidate [6]. It is the traditional electron source of rf vacuum electronics devices such as traveling wave tubes and klystrons used in radar, communications, and a variety of other commercial and military devices and systems for which ruggedness and reliability are paramount. The low work function coating on a dispenser cathode is maintained by the diffusion of, e.g., barium, to the surface of the cathode, replacing that which is lost due to desorption, evaporation, and sputtering [7], and such cathodes can be rehabilitated even when operating in nonideal conditions [8]. Compared to the work function of bare metals such as tungsten (4.63 eV for the 100 plane), the work function of a barium dispenser cathode is on the order of 2 eV, and scandate cathodes have shown an even lower work function of 1.8 eV [9]. An experimental program at the University of Maryland is investigating the performance of these cathodes as photoemitters. Here, theoretical models are developed and applied to experimental results previously reported [10]. The purpose of the models is, ultimately, to predict and extrapolate the performance of such cathodes in an FEL rf gun environment, where the laser intensities are orders of magnitude higher, the pulse lengths orders of magnitude shorter, and the applied fields larger, than are found in the present experimental arrangement.

*Also at Department of Electrical and Computer Engineering, University of Maryland, College Park, MD, USA.

Previously reported multiphoton emission experiments [11–18] have been on metals with work functions of 4–5 eV and for laser pulse lengths of 100–450 fs. In most of these studies, the incident lasers generated UV photons with energies greater than the work functions of the metals. Most of the previous studies reported only on the dependence of electron emission on incident laser intensity and were often primarily concerned with questions of either electron-electron and electron-lattice relaxation or direct photoemission. The present study addresses electron emission from a dispenser (low work function) cathode in which the incident photo energy is insufficient to produce direct photoemission until the electron gas is heated by the absorbed laser energy.

II. THEORETICAL MODEL

A. Laser heating of electron gas

A dispenser cathode consists of a matrix of micron-scale tungsten particles in a background of material containing a low work function impregnant such as barium which, under the application of heat, diffuses to and across the surface as a monolayer thick coating, and is subject to sputtering, desorption, and evaporation [19–21]. The majority of the cathode is therefore tungsten, and the surface layer can be initially disregarded in the estimation of the heating of the electron gas by the incident laser. The coupled differential equations relating the electron temperature T_e to the lattice temperature T_i are given by [17]

$$C_e \frac{\partial}{\partial t} T_e = \frac{\partial}{\partial z}\left(\kappa(T_e, T_i)\frac{\partial}{\partial z} T_e\right) - g(T_e - T_i) + G(z, t),$$
$$C_i \frac{\partial}{\partial t} T_i = g(T_e - T_i), \tag{1}$$

where G is the incident laser term, C_e and C_i are the electron and lattice heat capacities, g relates the energy per unit volume transferred by electrons to the lattice, and κ is the electron thermal conductivity. Other symbols are enumerated in Tables I and II. The specific heat capacity for electrons in a metal is given by (see, e.g., Ref. [22])

$$C_e(T) = \left(-k_B \beta^2 \frac{\partial}{\partial \beta}\right) \int_0^\infty (E - \mu) D(E) \times [1 + e^{\beta(E-\mu)}]^{-1} dE, \tag{2}$$

where $\beta = 1/k_B T$ and $D(E) = \eta m k(E)/(\pi\hbar)^2$ is the

TABLE I. Symbols and units.

Symbol	Definition	Value or unit
λ	Laser wavelength $= 2\pi\omega/c$	nm
T_0	Bulk temperature	Kelvin
β	Inverse electron temperature $= 1/k_B T_e$	1/eV
γ	C_e coefficient $\approx (\pi^2/3) k_B^2 D(\mu)$	$J/K^2\,m^3$
k	Wave number $= (2mE)^{1/2}/\hbar$	1/nm
I_0	Laser intensity	MW/cm^2
t_0	Laser pulse center parameter	ns
ϕ	Effective barrier height $= \Phi - \sqrt{(4QF)}$	eV

TABLE II. Parameters and values.

Symbol	Definition	Value
Φ	Dispenser cathode work function	1.8 eV
θ	Coverage factor	0.1278–0.3085
R	Reflectivity	50%
μ	Chemical potential	18 eV
δ	Photon penetration depth for tungsten	10.1 nm
Q	Image charge factor $e^2/16\pi\varepsilon_0 = \alpha_{Fs}\hbar c/4$	0.36 eV nm
A_0	Electron-electron relaxation time parameter	32.0514
λ_0	Electron-phonon relaxation time parameter	0.024 31
η	Tungsten thermal mass factor	1.203 76
Δt	Laser pulse width parameter	2.7 ns
λ	Laser wavelength $= 2\pi\omega/c$	1064 nm
ρ_0	(Number) density of tungsten	$(19.3\ g/cm^3)/(183.84\ g/mol)$
v_s	Sound velocity in tungsten	5220 m/s
g	Thermal energy transfer factor	$285.1\ GW/K\,cm^3$
γ	Specific heat coefficient at room temperature	$0.136\,48\ mJ/K^2\,cm^3$

density of states for unit volume, $\hbar k(E)$ is momentum, and the product ηm is the "thermal mass" of the electron. For simple metals, η is of order unity, but for transition metals, the d electrons contribute so that η can be larger; for tungsten $\gamma_{\rm exp} = C_e(T)/T = 136.48\ {\rm J/K^2\,m^3}$ [23], so that $\eta = \gamma_{\rm exp}/\gamma_{\rm theory} = 1.20376$, where $\gamma_{\rm theory} = mk_B^2 k_F/(3\hbar^2)$. For present parameters, $\beta\mu \gg 1$, and so

$$C_e(T) \approx \frac{k_B}{\beta}\int_0^{\beta\mu}\frac{y^2}{(e^y+1)(e^{-y}+1)}\left[D\left(\mu+\frac{y}{\beta}\right) + D\left(\mu-\frac{y}{\beta}\right)\right]dy = \frac{1}{3}\pi^2 D(\mu)\left[1-\frac{7}{40}\left(\frac{\pi}{\beta\mu}\right)^2-\frac{155}{896}\left(\frac{\pi}{\beta\mu}\right)^4\right], \quad (3)$$

where the second line results from Taylor expanding $D(E)$, and invoking the $W_+(n, \beta\mu)$ approximation for $\beta\mu \gg 1$ in Appendix A. Likewise, for the lattice,

$$C_i(T) = 9\rho_0 k_B\left(\frac{T}{T_D}\right)^3 W_-\left(4, \frac{T}{T_D}\right), \quad (4)$$

where ρ_0 is the (number) density of the metal, $T_D = (\hbar v_s/k_B)[\pi^2 r\rho_0]^{1/3}$ is the Debye temperature (400 K for tungsten [24], implying $r = 0.269701$), and $W_-(n, x)$ is defined in Appendix A. The thermal conductivity is given by

$$\kappa(T_e, T_i) = \frac{2\mu}{3m}\tau(T_e, T_i)C_e(T_e), \qquad \frac{1}{\tau} = \frac{1}{\tau_{ee}} + \frac{1}{\tau_{ph}}, \quad (5)$$

where the form for τ is due to Matthiessen's rule. The electron-electron and electron-phonon relaxation times are given by

$$\tau_{ee}(T_e) = \frac{\hbar\mu}{A_0}\left(\frac{1}{k_B T_e}\right)^2 = \frac{A_{ee}}{T_e^2},$$
$$\tau_{ph}(T_i) = \frac{\hbar}{2\pi\lambda_0}\left(\frac{1}{k_B T_i}\right) = \frac{B_{ep}}{T_i}, \quad (6)$$

where A_0 and λ_0 are dimensionless constants dictated by tungsten's bulk properties [17], in terms of which

$$g = \frac{\pi}{9\hbar}\lambda_0 m v_s^2 k_B k_F^3. \quad (7)$$

The behavior of the relaxation times is shown in Fig. 1. For steady-state conditions it follows that $T_e = T_i$, and so

$$\kappa = \frac{2\gamma\mu}{3m}(B_{ep} + A_{ee}T_e)^{-1}. \quad (8)$$

The term $G(z, t)$ constitutes the amount of energy absorbed by the lattice. It will be the product of several terms, namely, a factor related to the proportion of the laser reflected, the laser intensity, a factor governing the depth to which the incident photons are absorbed, and finally, a factor accounting for the fraction of photons not directly leading to photoemission, and is therefore given by

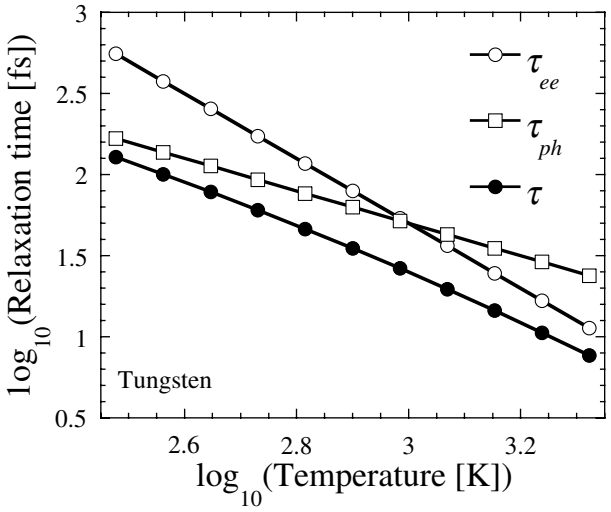

FIG. 1. Temperature dependence of the electron-electron and electron-phonon relaxation times, as per Eq. (6). The total relaxation time τ is obtained via Matthiessen's rule.

$$G(z, t) = (1-R)I_\lambda(t)\left(\frac{e^{-z/\delta}}{\delta}\right)\left[1-\frac{U[\beta(\hbar\omega-\phi)]}{U[\beta\mu]}\right],$$
$$I_\lambda(t) = I_0 e^{-[(t-t_0)/\Delta t]^2}, \quad (9)$$

where the $U(x)$ function and approximations to it are defined in Appendix B, R is the proportion of light reflected; t_0 is the center of the laser pulse; Δt is the laser time scale [i.e., $2[\ln(2)]^{1/2}\Delta t$ is the full width at half maximum (FWHM) of the laser pulse]; δ is the penetration depth of the incident photons of energy $\hbar\omega$; $\beta = 1/k_B T_e$; ϕ is the barrier height above the Fermi level and is given by $\phi = \Phi - (4QF)^{1/2}$, $(4QF)^{1/2}$ is the Schottky barrier lowering due to the image charge, and F (eV/nm) is the product of electric field and electron charge (and is therefore a *force*), other terms are defined in Tables I and II, and common symbols have their usual meanings (the methodology follows Ref. [25]). The quantity $\beta(\phi - \hbar\omega)$ is generally significant: at 300 K and no field for $\Phi = 1.8$ eV and $\lambda = 1064$ nm, it is equal to 24.6. The form of Eq. (9) is based on a thermalized Fermi-Dirac (FD) supply function (i.e., the FD distribution with momentum components parallel to the surface integrated out [25]). The square brackets containing the $U(x)$ terms acts as an "absorption factor," and its behavior is shown in Fig. 2 as a function of temperature for various wavelengths.

At present, Eq. (9) implicitly uses the Richardson approximation for the transmission probability, i.e., the electron is only transmitted, with unit probability, if its energy exceeds the surface barrier height $\mu + \phi$; the inclusion of quantum mechanical tunneling via a modified transmission probability calculation [26] will be deferred to a future work. It is assumed further that if an electron absorbs a photon such that its final kinetic energy exceeds the barrier height, it is emitted (analogous

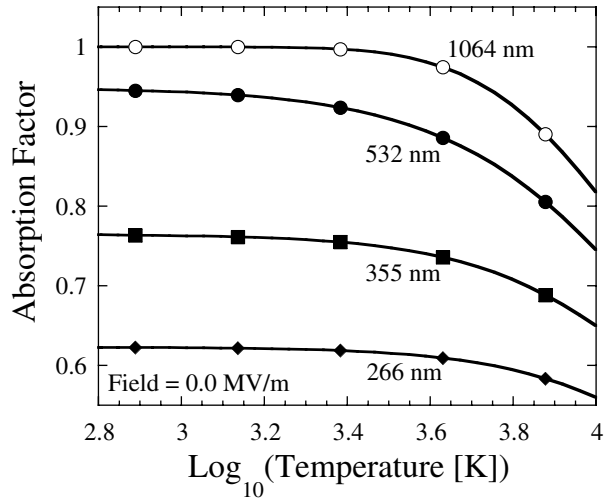

FIG. 2. Fraction of photons absorbed and leading to electron gas and lattice heating, corresponding to the term in square brackets of Eq. (9) for various wavelengths. For $\lambda = 1064$ nm, an electron at the Fermi level cannot surmount the barrier after photoabsorption. The decrease at higher temperatures is due to thermal spreading of the electron distribution. The temperature dependence of μ has not been taken into account.

to the approximations enumerated by DuBridge [27], and used, e.g., by Hernandez-Garcia and Brau [18]). For photon energies in excess of the work function, and using the asymptotic forms in Eq. (B5) of Appendix B, $U[\beta(\hbar\omega - \phi)] \propto (\hbar\omega - \phi)^2$, as found by Fowler [Eq. (7) of Ref. [34]] and commonly used [5]. Here, however, circumstances are different, in that the photon energy is less than the barrier height: as indicated by Fig. 2, the absorption factor is essentially unity over the fields and temperatures encountered for in the experimental conditions described below.

Other approximations are convenient. First, the time scale characteristic of the experimental laser pulse is 1 ns, but electron-electron and electron-phonon relaxation times are several orders of magnitude smaller so that the electron and lattice temperatures are in equilibrium, i.e., the steady-state approximation to Eq. (1) can be invoked which implies the electron and lattice temperatures are equal. Second, temperature decline into the bulk is governed by an exponential of the form

$$T_e(z) = T_0 + [T_e(0) - T_0]\exp\left(-\frac{z}{L}\right), \qquad (10)$$

where T_0 is the bulk temperature, and henceforth, $T_e = T_e(0)$ unless otherwise noted. The length scale is $L = n(\hbar k_F/m)\tau$, where k_F is the Fermi momentum, and the factor n—given that electron scattering will mimic a random walk—should be on the order of the square root of the ratio of the laser pulse time scale with the scattering time scale, or $n = (1\text{ ns}/0.1\text{ ps})^{1/2} \approx 100$. Equation (10), though reasonable, is nevertheless provisional: for shorter time scales, the actual spatial variation of the temperature should be found through a solution of the time-dependent Eq. (1) . Third, given that the cathode is predominantly tungsten grains, the heating of the electron gas by the laser can be approximated using bulk tungsten parameters. Invoking these approximations indicates that the electron temperature for ns-scale laser pulses is the solution of

$$\kappa\tau(T_e - T_0)\left(\frac{T_0}{\tau_{ph}} + \frac{T_e}{\tau_{ee}}\right) - T_e L^2 G_0(t) = 0, \qquad (11)$$

where $G_0(t) \equiv G(0, t)$, and henceforth $T_e \equiv T_e(0)$, (i.e., T_e refers to the temperature at the surface). It follows that the (surface) electron temperature at time t is the root of the equation

$$T_e^2(T_e - T_0) = \frac{3n^2}{\gamma}\left[\frac{G_0(t)}{B_{ep} + A_{ee}T_0}\right], \qquad (12)$$

where $\gamma = C_e(T_e)/T_e$, and is, to a good approximation, constant. When $G_0(t)$ is weakly dependent on temperature (as is true for experimental parameters considered herein), then T_e is the real root of a cubic equation and thereby easily determined. Observe, first, that Eq. (12) forces the electron temperature to have the same time dependence as the laser pulse, and second, that the simple form is a consequence of the approximation that the laser pulse time scale is much longer than the scattering relaxation times so that the lattice and electron temperatures are equivalent (a steady-state approximation). As a result, the equation will have to be modified when picosecond-length pulses are considered, a derivation deferred to a future work.

B. Photocurrent

The estimation of emitted current over the cathode contains several complications. Broadly, they are (i) nonuniform laser illumination resulting in a nonuniform temperature distribution across the surface, (ii) surface roughness inducing field enhancement, that is, the ratio of the field at the emission site to the macroscopic field is some factor greater than unity, and (iii) nonuniform coverage by the low work function coating. These complications are dealt with as follows. First, the actual laser profile is Gaussian in the cylindrical coordinate ρ; that is, $I_\lambda(\rho) = I_\lambda(0)\exp[-(\rho/\rho_0)^2]$, so that an "effective" emission area must be defined. Second, a surface analysis of the cathode revealed a lumpy surface with micron-feature sizes: a simple model of a nanoprotrusion on a bump easily generates enhancement factors $\beta_a = F_{\text{site}}/F_{\text{macro}}$ (where the subscript a on β_a is to distinguish it from the inverse temperature term, F_{site} is the field at the emission site, and $F_{\text{macro}} = F$ is the macroscopic field) on the order of 5 [25]. Finally, while models exist to predict work functions for partially covered surfaces, we shall opt to assume that a fraction θ of the cathode

is covered with a low work function coating, and a fraction $(1 - \theta)$ is bare metal (here, the work function of the bare metal is assumed constant and uniform, even though the variation of the work function with the crystal plane is a notoriously complicated affair: see Ref. [28]). For a new dispenser cathode at sufficiently high temperature, θ can approach unity, but as the coverage depends on temperature and operational history, effects of environmental degradation, and so on, for a mature cathode, it is smaller [7]. The emitted charge ΔQ from the cathode is then

$$\Delta Q = (\pi r_0^2) \int_{-\infty}^{\infty} [\theta J_\lambda(T_e(t), \Phi) + (1 - \theta) J_\lambda(T_e(t), \Phi_W)] dt, \quad (13)$$

where Φ_W = the work function of tungsten. The electron transmission probability for an incident energy E is a complex function [26], but if it is evaluated using the Richardson approximation, then the evaluation of Eq. (13) is considerably simplified. We find

$$J_\lambda(T, \Phi) = q(1 - R) \frac{I_\lambda(t)}{\hbar\omega} \left(\frac{U[\beta(\hbar\omega - \phi)]}{U[\beta\mu]} \right) + J_{\mathrm{RLD}}(T, \Phi),$$
$$J_{\mathrm{RLD}}(T, \Phi) = A_{\mathrm{RLD}} T^2 \exp[-\beta\phi], \quad (14)$$

where q is the electron charge, $A_{\mathrm{RLD}} = 120$ A/cm^2, $\phi = \Phi - \sqrt{(4QF)}$, and J_{RLD} is the Richardson-Laue-Dushman (RLD) equation [29]. Observe that β is time dependent because T_e depends on the laser intensity.

C. Quantum efficiency

The metric adopted for quantum efficiency herein is the ratio of the number of emitted electrons to the number of incident photons and is therefore given by $QE = [(\Delta Q/q)/(\Delta E/\hbar\omega)]$. Reflectivity of the surface, spatial variation of the incident laser, and other mitigating factors are therefore implicit. ΔQ is obtained from the time-integrated current, and ΔE from the time-integrated laser intensity. If both are Gaussian, then

$$QE_{1\mathrm{D}} = \frac{\hbar\omega}{q} \left(\frac{\mathrm{J}_\lambda(T_{\max})}{I_\lambda(0)} \right) \frac{\Delta t_e}{\Delta t_\lambda}, \quad (15)$$

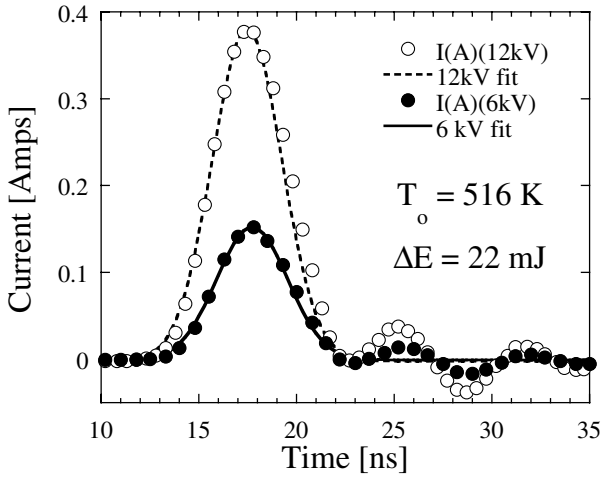

FIG. 3. Representative electron emission measurements for an incident laser striking a scandate dispenser cathode held at 516 K. Total time-integrated energy deposited is 22 mJ. The time scale of the Gaussian laser pulse is 2.7 ns. Anode potential was held at 12 kV (white dots) and 6 kV (black dots). The time scales of the Gaussian fits to the emission data are 2.52 and 2.57 ns, respectively.

where $T_{\max} = T(t = t_0)$, and Δt_e and Δt_λ are the Gaussian width parameters of the emitted electron (e) and incident laser (λ) pulses, respectively. For the laser, $\Delta t_\lambda = 2.7$ ns, the corresponding current parameter, though smaller and variable from measurement to measurement, is comparable, as shown in the typical example in Fig. 3, for which Δt_e is 93.2% and 95.5% of Δt_λ for the 12 and 6 kV curves, respectively. Henceforth, therefore, the ratio $\Delta t_e/\Delta t_\lambda$ shall be approximated by unity.

Unless the laser intensity is low, the thermal current J_{RLD} in Eq. (14) is negligible. Moreover, even at temperatures considered high from an operational standpoint, the quantities $\beta\mu$ and $\beta(\phi - \hbar\omega)$ are relatively large so that the asymptotic limits of Eq. (14) dominate, e.g., for $T = 2000$ K, $F = 2.55$ MeV/m, $\Phi = 1.8$ eV, and $\lambda = 1064$ nm, then $\beta\mu$ and $\beta(\phi - \hbar\omega)$ are 33.95 and 3.331, respectively. It follows that

$$\lim_{\substack{\beta(\phi - \hbar\omega) \to \infty \\ \beta\mu \to \infty}} J_\lambda(T, \Phi) \Rightarrow (1 - R) \frac{(2\pi\hbar)^2}{m\omega\mu^2} I_\lambda(t) J_{\mathrm{RLD}}(T, \phi - \hbar\omega). \quad (16)$$

Consequently, the total emitted charge will be dominated by the maximum temperature region occurring near $t = t_0$. It is therefore reasonable to expect that the total emitted charge ΔQ will be approximately linear on a Richardson plot in which $\ln[\Delta Q/T_{\max}^2]$ is plotted as a function of $1/T_{\max}$, where $T_{\max} = T_e(t_0)$. Conversely, when the wavelength is small, then the photon energy exceeds the barrier height, that is, $\hbar\omega > \phi$ and so

$$\lim_{\substack{\beta(\hbar\omega - \phi) \to \infty \\ \beta\mu \to \infty}} J_\lambda(T, \Phi) \Rightarrow \frac{q}{\hbar\omega} (1 - R) I_\lambda(t) \left(\frac{\hbar\omega - \phi}{\mu} \right)^2. \quad (17)$$

Equation (14) suggests that the time-dependent quantum efficiency $QE(t)$ is given by the ratio of the U functions. Using the asymptotic expressions in Eqs. (14) and (17) gives (surface coverage factors not included)

$$QE_{\mathrm{1D}} \approx \begin{cases} 2(1-R)(\frac{k_B T}{\mu})^2 \exp[-(\phi-\hbar\omega)/(k_B T)] & [\beta(\hbar\omega-\phi) \Rightarrow -\infty], \\ (1-R)(\frac{\hbar\omega-\phi}{\mu})^2 & [\beta(\hbar\omega-\phi) \Rightarrow \infty], \end{cases} \tag{18}$$

with the proviso that when the difference between the photon energy and the barrier height exceeds the chemical potential, QE_{1D} is unity. Note that $T = T(t)$ and depends on the laser pulse profile. The average quantum efficiency will then be a fraction of the maximum QE. It is important to emphasize that QE_{1D} for arbitrary wavelength must be evaluated using Eq. (B5) to evaluate the U ratios, especially when there is spatial and/or temporal variation of the incident laser as well as nonuniformity of the emitting surface. In such cases, the *average* quantum efficiency is evaluated using ratios of the spatiotemporal averaged values of J_λ/q and $I_\lambda/\hbar\omega$, and is taken up below.

D. Relation of theory to experiment

The (dimensionless) independent parameters that govern the agreement with experimental data using Eq. (13), and their anticipated magnitudes, are (i) the factor $n =$ O(100) in the temperature variation length scale parameter L, (ii) the field enhancement factor $\beta_a =$ O(5), and (iii) the surface coverage factor $\theta =$ O(0.1). The experimental parameters that are varied and which therefore determine these quantities are the laser intensity I_0 (MW/cm^2), the macroscopic field F/q (MV/m), and the bulk temperature T_0 (K). The quantum efficiency of various metals reported in the literature serve as an independent confirmation of the values identified herein. Parameters which are unknown or in principle unknowable, such as the exact value of the reflectivity R and the work function Φ at the emission sites, the proportion of the emission sites participating in the emission process, the thermal factors associated with the impregnates between the tungsten grains in the dispenser cathode, and the like, generally appear in conjunction with the chosen independent parameters. We therefore choose appropriate generic parameters for these quantities, as in the case of $R = 50\%$ and $\Phi = 1.8$ eV, or treat the adjustables as *effective* parameters, as in the case of β_a and θ.

III. EXPERIMENTAL AND SIMULATION RESULTS

A. Experimental procedure

Scandate cathodes fabricated by Spectra-Mat Inc. [30] were illuminated by a Q-switched Nd:YAG laser generating Gaussian pulses with FWHM equal to $2[\ln(2)]^{1/2}\Delta t_\lambda = 4.5$ ns. The field between the cathode and anode was varied from 0 to 2.5 MV/m. The laser was focused to a circular spot on the cathode with a FWHM area of approximately 0.3 cm^2. The photon energies/wavelengths of the 2nd, 3rd, and 4th harmonics of the Nd:YAG laser are 2.33 eV/532 nm, 3.50 eV/355 nm, and 4.66 eV/266 nm, respectively. The corresponding QE were found to be 6.5×10^{-5}, 2×10^{-4}, and 8×10^{-4}. The electron emission exhibited "normal" photoemission characteristics; that is, the emission was proportional to the incident laser intensity and independent of the low electric field gradients (0.1 to 2.0 MV/m).

As reported earlier, a very different behavior was observed when the Nd:YAG fundamental (1.165 eV, 1064 nm) was used [10]. The electron emission was highly nonlinear with respect to illumination intensity and strongly dependent on both the electric field gradient and the temperature of the substrate lattice. Figure 3 shows representative behavior of experimental data readings: the symbols correspond to the experimental data points, whereas the lines correspond to a curve fit of the form

$$I_q(t) = I_q^0 \exp\{-[(t-t_0)/\Delta t]^2\} + I_{\mathrm{base}}, \tag{19}$$

where I_q is a current, not a laser intensity, I_{base} is a background current, and the oscillations after the pulse are artifacts of the circuit used to measure the emitted charge. The emitted charge is then approximated by $\Delta Q = \pi^{1/2} I_q^0 \Delta t$. Figure 4 shows several such

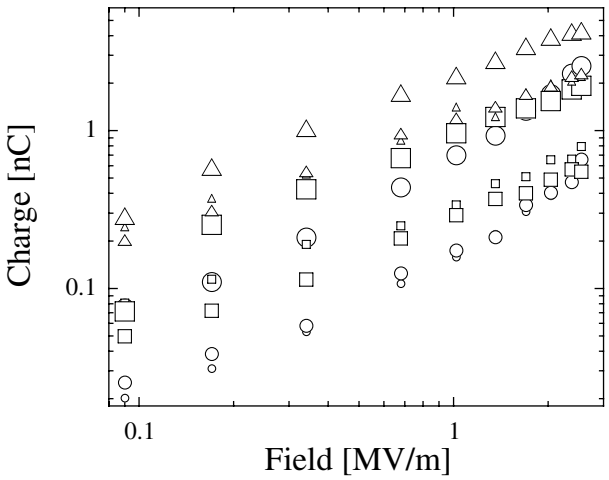

FIG. 4. Experimental total emitted charge versus applied field for various bulk temperatures and deposited energy values. Small symbol to large symbol referred to 12, 16, and 22 mJ, respectively, of deposited laser energy. Circles, squares, and triangles referred to 516, 618, and 713 K bulk temperature values, respectively. The general trend is greater emitted charge for increasing applied field, temperature, and laser intensity, as expected.

measurements taken over the course of weeks, for temperatures of 516, 618, and 713 K (circle, square, and triangle, respectively) for deposited laser energies of 12, 16, and 22 mJ (small to large symbol, respectively) over a range of fields. In the course of obtaining measurements, the cathode was continually refurbished on a daily basis, and it appears likely that the cathode did not return to the same condition over time, e.g., the degree of coverage might have evolved or alignment of the laser spot on the cathode might occur on a different region of the surface. Some degradation in performance was generally observed following conditioning. It is therefore quite unlikely that a single set of theoretical parameters will suffice to model the experimental data sets *in toto*. Nevertheless, the degree to which these parameters do vary can serve to assess how well the model is performing.

B. Measurement considerations

Other complications which impact the one-dimensional theoretical model presented above are (i) laser intensity variation, (ii) macroscopic field variation, and (iii) subsequent temperature variation across the surface. Regarding the laser intensity $I(\rho) = I_0 \exp[-(\rho/\rho_0)^2]$, simulation took as the emission area the disk defined by $(\rho/\rho_0)^2 = 2$ so that for a FWHM illumination radius corresponding to an area equal to 0.3 cm^2, $\rho_0 = 0.354$ cm, implying the simulation radius is 0.5249 cm. If a smaller simulation radius were chosen, e.g., ρ_0 itself or $\sqrt{2}\rho_0$, the estimates for θ would be increased, and a slight decrease in the value of $L(n)$ would also result. Regarding field variation, the cathode was a 1.27 cm diameter rod. The anode was a tube with a 1.27 cm inner diameter and a 2.54 cm outer diameter. The edges of the anode facing the cathode were rounded and sat inside a dielectric tube with an inner diameter of 3.175 cm. The anonde-cathode separation was approximately 0.4 cm. The electrostatic program POISSON was used to calculate the fields when no current was drawn. With a 1 kV anode potential, the tangential and perpendicular fields were, at the center, 0 and 0.17 MV/m, respectively, while at the edge (where the laser illumination was weak), they were 0.2 and 0.45 MV/m, respectively. Finally, the electron temperature is the greatest where the laser intensity is strongest (near the center of the beam spot): for the 1D theory results, the effective coverage factor θ will therefore be lower than the actual.

C. Comparison of theory to experiment

Experimental parameters are such that initially, no significant photoemission occurs when the 1064 nm laser light is incident on the cathode, as the barrier height exceeds the photon energy for all electron energies appreciably present in the electron distribution: that is, $\Phi - (4Qb_aF)^{1/2} - \hbar\omega \approx 0.5135$ eV for $F/q = 2.55$ MV/m $= 2.55 \times 10^{-3}$ V/nm and a field enhancement of $\beta_a = 4$.

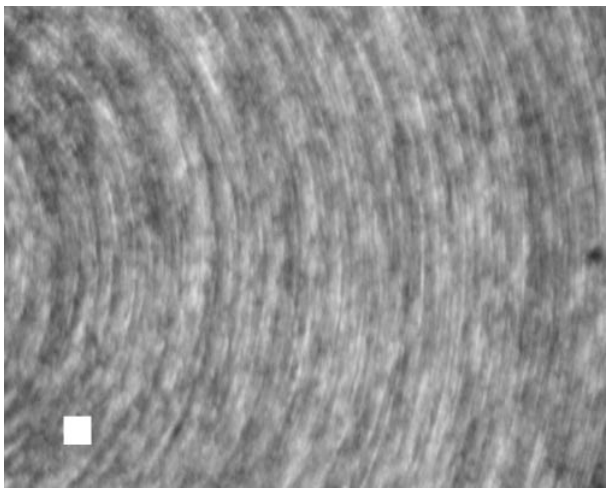

FIG. 5. Photograph of the scandate dispenser cathode surface. Concentric rings are evident from machining. The white square in the lower left corner corresponds to a 0.1 mm $\times$ 0.1 mm area.

The reasonableness of the field enhancement factor selected is indicated in Fig. 5, which shows an image of the surface (the white square representing an area 100 μm on a side), cross-section profilimetry plots in Figs. 6 and 7 at two radial length scales, and the observation that the field enhancement factor for a simple hemisphere is 3.0.

Measurements of emitted charge were taken as a function of the total deposited energy ΔE, macroscopic field, and bulk temperature. Typical experimental results are shown in Figs. 8–10. In Fig. 8, the variation of current (related to ΔQ) with incident laser power (related to ΔE) at a field of 1.7 MV/m and lattice temperature of 300 K is shown (the black dot corresponds to the 1064 nm data point in Fig. 13). The current shown is an "average"

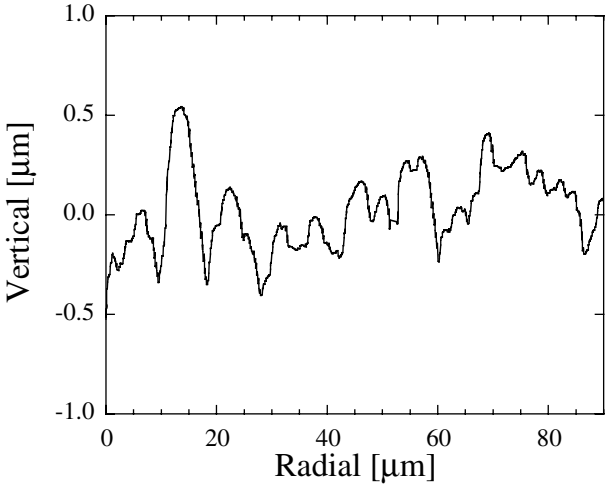

FIG. 6. A surface height plot of the scandate cathode shown in Fig. 5 as a function of the radial coordinate. The radial "origin" does not correspond to the center of the cathode.

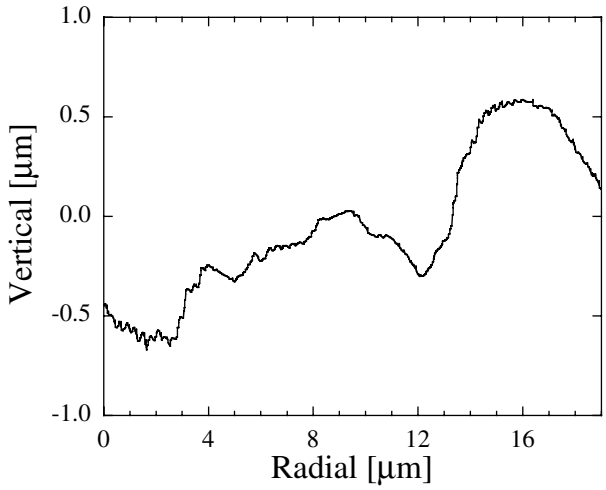

FIG. 7. Same as Fig. 6, but showing greater detail in the radial direction. Note the presence of nanoprotrusions which provide field enhancement apart from the larger scale features.

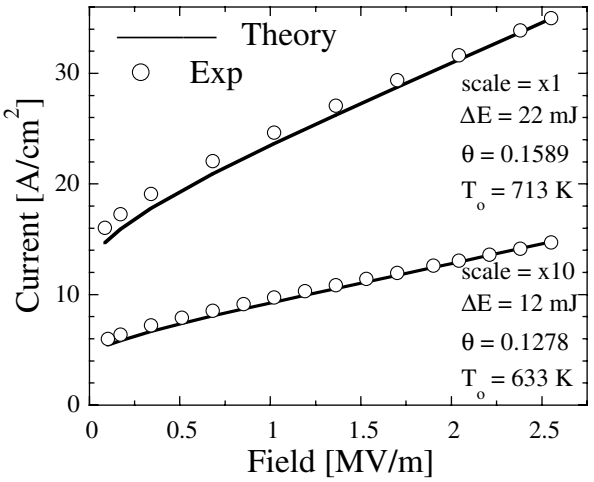

FIG. 9. Same as Fig. 8, but as a function of macroscopic field due to changes in anode potential for two cases: 22 mJ of laser energy for a bulk temperature of 713 K, and 12 mJ of laser energy for a bulk temperature of 633 K. Note that the surface coverage factor θ changes.

current density, given by the ratio of the total emitted charge to the FWHM time and area factors (4.5 ns and 0.3 cm^2, respectively). In Fig. 9, ΔQ is shown as a function of the electric field gradient variation for a laser intensity of 15 MW/cm^2 and bulk temperature of 713 K for two different intensities; for the lower intensity (denoted by $\Delta E = 12$ mJ), the values have been scaled by a factor of 10 to render them discernible. Finally, Fig. 10 shows the variation with temperature for a field of 1.7 MV/m and laser intensity of 6 MW/cm^2. By using the 2nd harmonic light, it was determined that these measurements were not field limited, as the subsequent photoemission was not a function of field gradient.

All parameters used in the theoretical model are based on bulk tungsten except for the effective work function Φ, field enhancement factor β_a (dimensionless), the length scale $L(n)$, and the surface coverage factor θ (dimensionless). The theoretical estimate of ΔQ for Fig. 8 was satisfied by the parameters $\beta_a = 4.0$, $n = 26.81$, and $\theta = 0.3085$. For Fig. 9, because the cathode performance changes with time (the cathode was continually "refurbished" by heating over the course of the experiments so that the same surface coverage factor did not necessarily obtain from figure to figure), only θ was allowed to change, as it is unlikely that β_a and n would (see the quantum efficiency and bare metal results below). The theory assumed that θ degraded from 0.3085 to 0.1589 and 0.1278 for $\Delta E = 22$ mJ and 12 mJ, respectively. For Fig. 10, no further adjustments were made, so that the

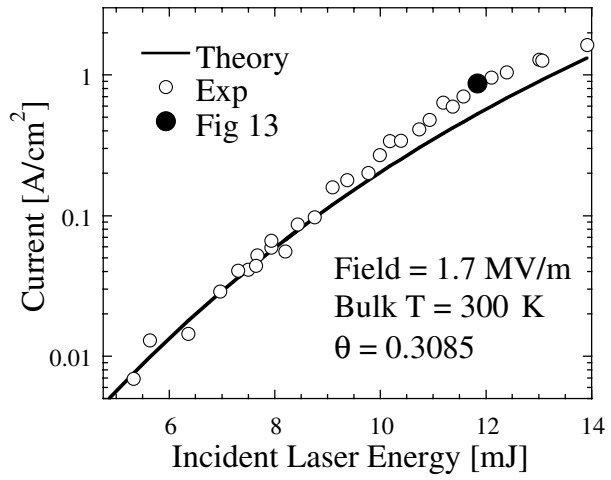

FIG. 8. Comparison of experimental data with simulation for emitted charge versus incident laser energy for Table II parameters and values shown. Laser wavelength was 1064 nm. The black dot corresponds to the dot indicated in Fig. 13.

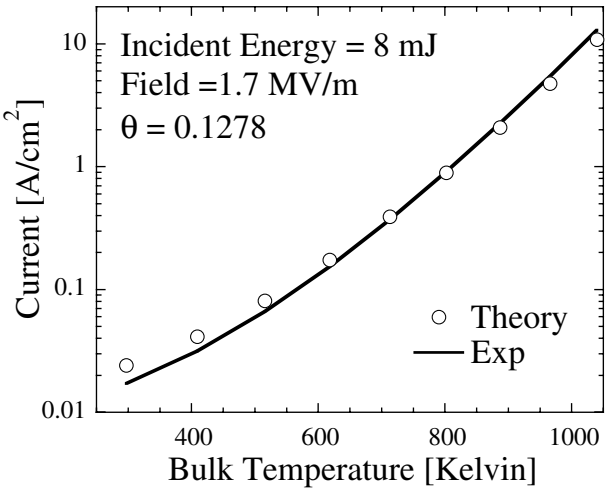

FIG. 10. Same as Fig. 8, but as a function of bulk temperature for a fixed laser intensity and applied field. The same coverage factor as in the 12 mJ case of Fig. 9 was used.

value of θ was taken from the 12 mJ case of Fig. 2 (8 mJ being closer to 12 mJ than 22 mJ). In Fig. 11, ΔQ is shown on a Richardson plot vs $1/k_B T_{\max}$, for Fig. 8 parameters: While some convexity is apparent, the resulting plot is predominantly linear, reflecting the expectation generated by Eq. (16). The convexity is likely due to nonlinearities in $T(\Delta E)$ with temporal and spatial variations in the incident laser intensity.

D. Quantum efficiency revisited

Two issues immediately present themselves: first is the reasonableness of the n factor, which contributes to the value of $L(n)$ and which can be assessed from quantum efficiency estimates; and second is the extension of the QE_{1D} formula to a situation in which the incident laser is spatially and temporally varying (e.g., a Gaussian in ρ and t).

Regarding the n factor, the formula for QE_{1D} can be used to "predict" the work function of bare metals, once the quantum efficiency of those metals is established. We consider two cases: first, bare tungsten, as tungsten constitutes the "bulk" material in the simulation of the dispenser cathode discussed above, and second, gold, as that metal is "simple" in that thermal mass effects do not arise in the evaluation of $C_e(T)$. QE estimates can be deduced from the slope of the $N = 1$ in the photoelectron current density plots ("Au" and "W" of Fig. 1 of Papadogiannis *et al.* in Ref. [17]), from which we deduce that $QE(\mathrm{W}) = 3.49 \times 10^{-5}$ and $QE(\mathrm{Au}) = 7.54 \times 10^{-6}$ (comparable to the findings of Logothetis and Hartman [11]). Simulations were run with the parameters given in Table III for a range of work functions. The resulting quantum efficiency was deduced from

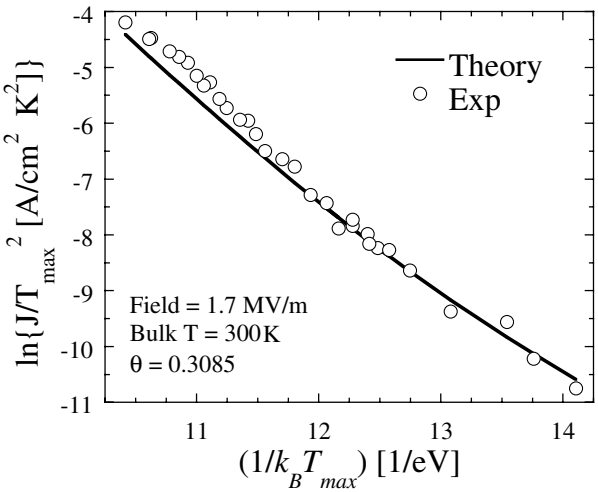

FIG. 11. Same as Fig. 8, but on a Richardson plot in which $\ln Q/T^2$ is plotted versus $1/T_{\max}$, where $T_{\max}$ is evaluated via Eq. (12), showing approximate linearity and indicating thermal-emission-like behavior.

TABLE III. Material parameters.

Symbol	Tungsten	Gold
μ	18.08 eV	5.51 eV
A_0	32.0514	4.8839
λ_0	0.024 313	0.121 57
T_0	300 K	300 K
F/q	0.0 MV/m	0.0 MV/m
δ	10.1 nm	25.7 nm
η	1.203 76	1.0
ΔE	0.001 mJ	0.001 mJ
θ	1.0	1.0
R	50%	50%
λ	266 nm	266 nm
n	26.809	26.809

$$QE = \frac{\hbar\omega}{q}\left(\frac{\Delta Q}{\Delta E}\right) = 1.2398 \times 10^{-3}\left(\frac{\Delta Q[\mathrm{nC}]}{\lambda[\mathrm{nm}]\Delta E[\mathrm{mJ}]}\right). \tag{20}$$

The results of the simulation are shown in Fig. 12. The parameters followed the dispenser cathode simulations except the laser intensity was reduced to eliminate a thermal emission component of the current, the applied field was eliminated to avoid complications due to Schottky factors, and the wavelength was taken to be UV. It is seen that the "predicted" work function values $\Phi(\mathrm{W}) = 4.52$ eV and $\Phi(\mathrm{Au}) = 4.69$ eV based on the quantum efficiency estimates for n fall close to photoelectric work function values generally attributed to tungsten and gold [31], as shown in the Table inset of Fig. 12.

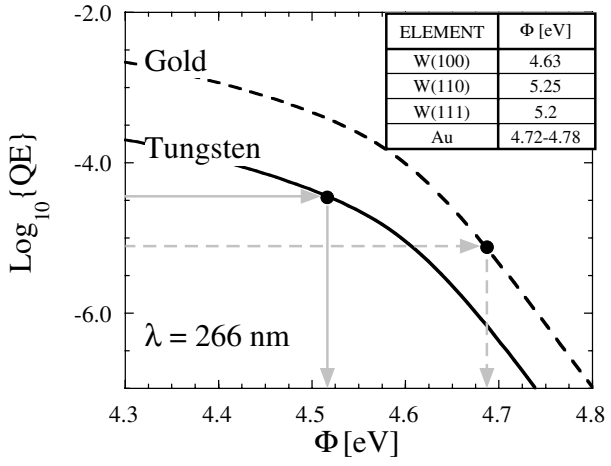

FIG. 12. "Predicted" work functions for bare metals tungsten and gold based on Table III parameters. The simulation code developed to treat the dispenser cathode can be used to predict work function based on quantum efficiency once an estimate of $L(n)$ is available. The agreement between theory and experiment for several materials suggests the value of n is reasonably generic.

Consequently, though n was chosen to provide a correspondence with the dispenser cathode simulations, its value was independently shown to be appropriate for bare metal simulations and is therefore reasonable.

Regarding the laser spot, due to the exponential relationship between T and J_{RLD}, only a portion of the illuminated region shall be emitting to any significant extent, and as a consequence of the temporal variation of the laser pulse, it shall emit only for a finite time. Consequently, for the 2D problem characterizing the laser-cathode interaction, the analog of the 1D quantum efficiency estimate, codified in Eq. (18), requires modification to account for the spatiotemporal nature of the illumination. The appropriate generalization to QE_{1D} is

$$QE_{\mathrm{2D}} = \theta(1-R)\frac{\frac{1}{q}\int_{-\infty}^{\infty} dt \int_0^{\infty} 2\pi\rho d\rho J_{\lambda}[t,\rho,T(t,\rho)]}{\frac{1}{\hbar\omega}\int_{-\infty}^{\infty} dt \int_0^{\infty} 2\pi\rho d\rho I_{\lambda}(t,\rho)}, \tag{21}$$

where the explicit dependence of the temperature on time and position (as a consequence of changes in laser intensity) is shown. Asymptotic limits can be obtained using the limits of QE_{1D}. Recall that the laser variation is Gaussian in both time t and axial coordinate ρ with corresponding scale parameters Δt and ρ_0, respectively. The independence of $QE_{\mathrm{1D}}(\hbar\omega \gg \phi)$ from t and ρ follows from its lack of temperature variation, so that

$$\lim_{\beta(\hbar\omega-\phi)\to\infty} QE_{\mathrm{2D}} = \theta(1-R)\left(\frac{\hbar\omega-\phi}{\mu}\right)^2. \tag{22}$$

The case ($\hbar\omega < \phi$) is more difficult because of the dependence on bulk temperature. Using the dimensionless parameters $x = (\rho/\rho_0)$ and $s = (t-t_0)/\Delta t$, it follows that

$$\lim_{\beta(\phi-\hbar\omega)\to\infty} QE_{\mathrm{2D}} = \theta(1-R)QE_{\mathrm{1D}}(T_{\max})\frac{\int_{-\infty}^{\infty} ds \int_0^{\infty} xdx \exp[-(w+1)(s^2+x^2)]}{\int_{-\infty}^{\infty} ds \int_0^{\infty} xdx \exp[-(s^2+x^2)]} = \theta(1-R)\frac{QE_{\mathrm{1D}}(T_{\max})}{(w+1)^{3/2}}, \tag{23}$$

where w is determined from the spatial and temporal variation of the temperature T and the approximation $\ln[J_{\mathrm{RLD}}(T)/J_{\mathrm{RLD}}(T_{\max})] \approx -w(s^2+x^2)$. To leading order

$$w \approx \frac{1}{3}\left(1-\frac{T_0}{T_{\max}}\right)\left(2+\frac{(\phi-\hbar\omega)}{k_B T_{\max}}\right), \tag{24}$$

where the (1/3) coefficient nominally accounts for Eq. (12). The performances of Eqs. (22) and (23) are shown in Fig. 13 compared to experimental findings, including the quantum efficiency value for the shorter wavelength. The $\lambda = 1064$ nm case depends on the laser intensity and the bulk temperature, and consequently depends on initial conditions, whereas the shorter wavelength cases are asymptotically independent of the intensity and bulk temperature.

The quantum efficiencies shown in Fig. 13 for present experimental conditions are not sufficient to generate interest, a consequence of the diminutive laser intensity: sufficient electron temperatures are not generated to produce interesting emission levels. In device application, however, laser intensities will be much higher. It is therefore germane to investigate the consequences of higher intensities (achieved in the simulation by considering shorter 2.7 ps pulses for a given ΔE, which is still sufficiently long in comparison to the total relaxation time). Two cases are considered: a simple extrapolation of the cathode described above and a hypothetical cathode whose surface has been planarized (no field enhancement effects, $\beta_a = 1.0$) but which has an effective surface coverage comparable to standard mature thermionic dispenser cathodes (i.e., $\theta = 0.60$ and a uniform laser illumination) at the same macroscopic field of 2.55 MV/m. The results are shown in Fig. 14, where the laser intensity is constrained such that the electron/lattice temperature remains approximately 300 K below the melting point of tungsten (3683 K). Quantum efficiencies between 0.83% ($\beta_a = 4.0$, $\theta = 0.3085$) and 1.3% ($\beta_a = 1.0$, $\theta = 0.6$) are found for the highest laser intensity considered (white dot, white square, respectively). Continuing, we consider wavelengths characteristic of a Ti:sapphire laser, i.e., $\lambda = 800$ nm (black dot) at the same field of

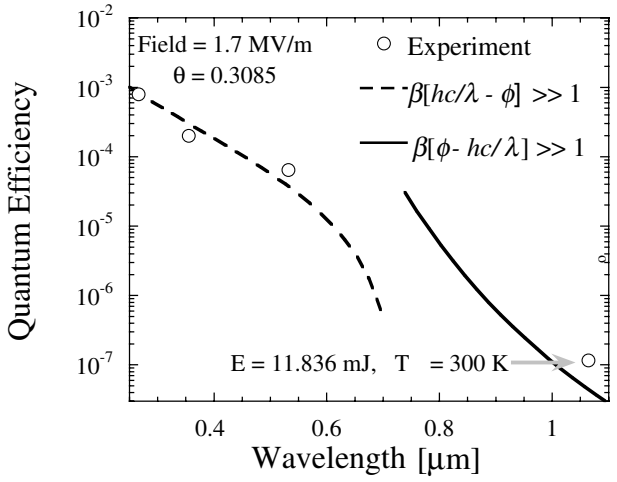

FIG. 13. Measured quantum efficiencies compared to the asymptotic formulas of Eq. (18). Dot indicated by arrow corresponds to the black dot in Fig. 8.

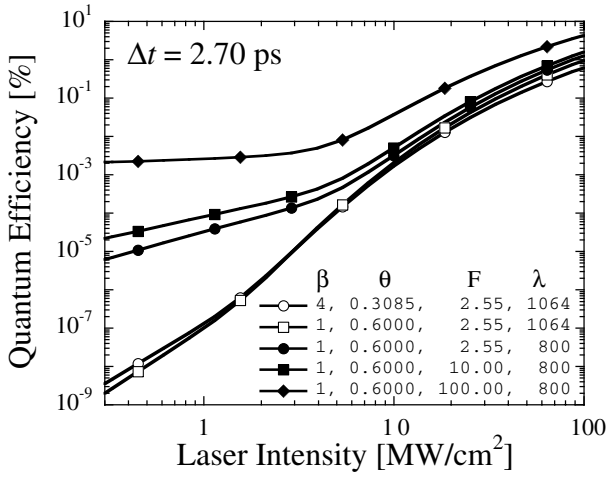

FIG. 14. Quantum efficiency for experimental parameters and its projection for higher laser power and surface coverage factors. Factors not explicitly listed are presumed the same as in Table II.

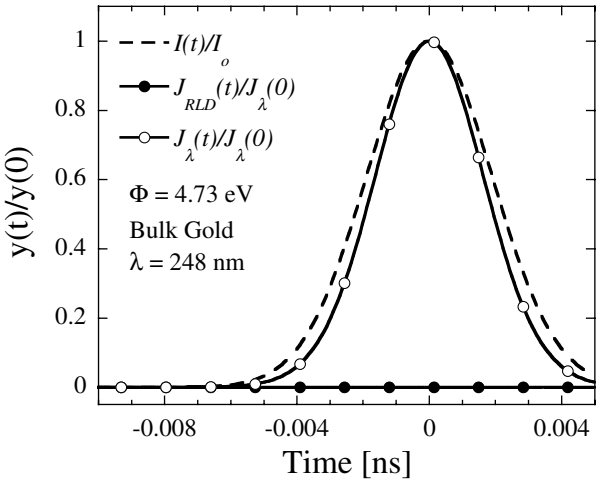

FIG. 15. Comparison of the laser pulse shape with the emitted charge pulse shape for gold (Table III) parameters, UV light (266 nm), $\Delta E = 1.0$ mJ, and $\Delta t = 2.7$ ps. J_{RLD} is the Richardson equation for a time-dependent electron temperature. It is seen that thermal emission due to electron gas heating does not appreciably occur for these values.

2.55 MV/m, but also higher fields characteristic of Naval and accelerator applications (10 MV/m—black square, and 100 MV/m—black diamond, respectively), where the impact of Schottky barrier lowering becomes increasingly evident (the barrier lowering is 0.038 eV for a field of 1 MV/m). The corresponding increase in current (and hence, QE), as per the RLD equation, scales by a factor of $\exp[\beta\sqrt{(4QF)}]$: for temperatures of 1000, 2000, and 3000 K, such factors are (for 10 MV/m) 4.02, 2.00, and 1.59 for 10 MV/m and (for 100 MV/m) 81.7, 9.04, and 4.34, respectively. It is clear that QE's of technological interest are indicated.

E. Thermal and field-assisted photoemission

A short, intense pulse at UV on a bare metal such as gold or tungsten will have a different signature than a long pulse on a low work function dispenser cathode, as a consequence of Eq. (13). Consider $\Delta E = 1$ mJ for a $\lambda = 266$ nm laser incident on gold, with a pulse width of $\Delta t = 2.7$ ps corresponding to a laser intensity of 0.116 GW/cm^2 for the spot size considered. A fraction of the emitted electrons will be due to direct photoemission, and a fraction due to thermal emission from the heated electron gas (recall that the bulk of the laser energy is absorbed and dissipated into heat), as per Eq. (14). For bare metals, the work function is sufficiently high that no appreciable thermal component contributes, and the photon energy is so large that the electron pulse closely follows the laser pulse in shape, as in Fig. 15. Two differences arise for low work function/long wavelength cases, depending on whether the pulse is long or short, for a given deposited ΔE. If the pulse is long (ns scale), then the electron temperature remains such that the thermal emission component is not appreciable, and the bulk of the emitted current is due to photoemission from a hot electron distribution, as in Fig. 16. If the pulse is short (ps scale), then the electron temperature can markedly rise, indicating that the thermal component can become substantial and constitute the bulk of the emitted current, as a consequence of the low work function, as in Fig. 17. In both cases, note that the width of the electron pulse is shorter than that of the laser pulse, due to the steep temperature dependence of the emitted current. For a given ΔE, the quantum efficiency of a dispenser photocathode is, therefore, substantially enhanced by the thermal current component for short (intense) pulses in distinction to what would be extrapolated from efficiency estimates based on longer (less intense) laser pulses producing electron emission dominated by the

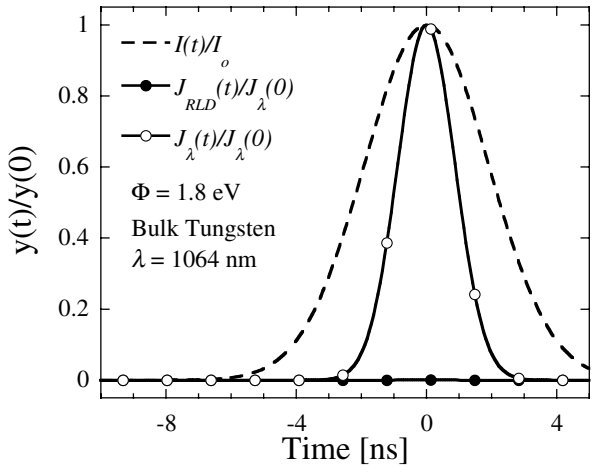

FIG. 16. Same as Fig. 15, but for long wavelength (1064 nm), work function of a scandate cathode, $\Delta E = 1.0$ mJ, and $\Delta t = 2.7$ ns.

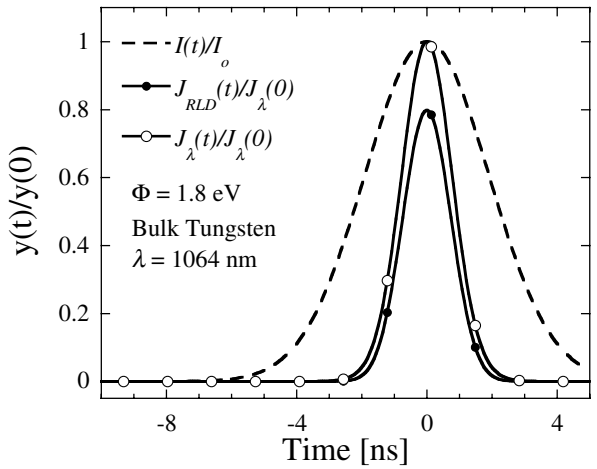

FIG. 17. Same as Fig. 16, but for an incident laser intensity a factor of 10 higher ($\Delta E = 10$ mJ). The electron temperature now significantly increases, giving rise to a large thermal component of emitted charge.

photoemission from a heated electron gas. Moreover, the Schottky factor induced by the applied field contributes significantly. At very high laser intensities, nonlinear effects come into play (see the $N \geq 2$ regions of Fig. 1 in Ref. [17]) and complicate this description.

IV. CONCLUSION

We have provided a model for the interpretation of experimental data of electron emission from a laser-illuminated dispenser cathode. Issues were identified in the relation between the theoretical model and its application to the experimental data. First, surface roughness always exists, so some field enhancement is always present and will make the emission higher. Second, the exact degree of surface coverage will depend on environment, contaminants, temperature, and surface conditions, and is therefore difficult to surmise without reference to experimental data. Third, invoking a steady-state approximation to model electron heating by the laser is tantamount to keeping the electron and lattice temperature in equilibrium throughout the pulse: for pulses in which the pulse length is comparable to the relaxation time, decoupling will occur, and the electron temperature will be higher than the lattice, increasing the emission. Fourth, for such low work functions, some quantum mechanical tunneling current will be present, and the thermionic current at the barrier maximum will be overestimated. Fifth, for short pulses, heat propagation into the bulk will differ from the exponential decay used herein: presumably, the electron temperature will therefore be larger near the surface. Sixth, the dispenser cathode barrier has been treated as an image-charge lowered standard metal-like barrier, whereas in fact barrier lowering is accomplished by the influence of dipoles at the surface: it is unclear at the present stage of development what impact a proper account of the barrier will have on the estimation of emitted current. An accurate account of these six issues necessitates a time-dependent simulation code to monitor heat propagation into the bulk, the efficiency of energy transfer from electrons to lattice, and a proper account of the emission barrier. We are presently undertaking the development of this model and its numerical implementation and seeking to validate it by comparing its predictions to other dispenser cathode technologies.

In summary, we have shown that the theoretical model of a laser-heated electron gas giving rise to photothermal emission is consistent with experimental findings of infrared laser illumination of a scandate dispenser cathode. The surprisingly good quantitative agreement between experiment and simulation bodes well for theoretical extrapolation to parameters not achieved experimentally but nevertheless representative of future devices. Based on findings herein, the dispenser cathode technology appears to offer promise as a phototocathode candidate. The temporal characteristics of the laser and the limitations of the test cell in the present study constrain the power density and electric fields achieved to well below those characteristic of an rf photoinjector. Even though the laser time scale was in the nanosecond regime, the relevant relaxation times which equilibrate the electron and lattice temperatures are in the subpicosecond regime for metals [13], and so the modeling of the experimental data may proceed using a steady-state formulation. Significantly, however, picosecond and femtosecond pulses allow much higher laser intensity damage thresholds, and those times are in the range of electron-phonon relaxation times. To obtain information relevant to devices, the theory will be extended to the short pulse time-dependent regime, and experiments will be carried out using shorter pulse lasers. Finally, extrapolations based on the present study clearly indicate that dispenser cathodes function as a promising photoemitter source.

ACKNOWLEDGMENTS

We most gratefully acknowledge funding for this work provided by the Joint Technology Office and the Office of Naval Research. We have benefited from discussions with Arnold Shih, Joan Yater, Jonathan Shaw, and Robert Parker (NRL), and David Demske and Jon Neumann (UMD).

APPENDIX A: APPROXIMATION TO FERMI-DIRAC AND BOSE-EINSTEIN INTEGRALS

The evaluation of the specific heat capacity expressions results in an encounter with integrals of the form

$$W_{\pm}(n, x) = \int_0^x \frac{y^n}{(e^y \pm 1)(\pm e^{-y} + 1)}\, dy, \qquad \text{(A1)}$$

where W_+ corresponds to electrons and W_- to phonons,

reflecting the difference between Fermi-Dirac and Bose-Einstein statistics. From the general result [32]

$$\int_0^1 \frac{[\ln(x)]^n}{1 + 2x\cos(t) + x^2}\,dx = \frac{n!}{\sin(t)}\sum_{k=1}^{n}(-1)^{n+k-1}\frac{\sin(kt)}{k^{n+1}} \tag{A2}$$

and the special cases

$$W_{\pm}(n, \infty) = n!\zeta(\mp n), \tag{A3}$$

where $\zeta(-n) = (1 - 2^{1-n})\zeta(n)$ is the Riemann zeta function [33]; it follows that adequate approximations for numerical work, valid for $n \geq 2$, are available from the first few terms in the series expansion given by

$$W_+(n, x) = \begin{cases} \left(n!\zeta(-n) - \frac{x^n}{e^x+1} - n!\sum_{h=1}^{n}\sum_{j=1}^{\infty}\frac{(-1)^{j-1}e^{-jx}x^{n-h}}{(n-h)!j^h}\right) & x > 1, \\ \left(\frac{x^{n+1}}{4(n+1)}\left[1 - \frac{(n+1)}{4(n+3)}x^2 + \frac{(n+1)}{24(n+5)}x^4\right]\right) & x < 1, \end{cases} \tag{A4}$$

and

$$W_-(n, x) = \begin{cases} n!\zeta(n) - \left(\frac{x^n}{e^x-1} + n!\sum_{h=1}^{n}\sum_{j=1}^{\infty}\frac{e^{-jx}x^{n-h}}{(n-h)!j^h}\right) & x > 1, \\ \left(\frac{x^{n-1}}{(n-1)}\left[1 - \frac{(n-1)}{12(n+1)}x^2 - \frac{(n-1)}{240(n+3)}x^4\right]\right) & x < 1. \end{cases} \tag{A5}$$

The Riemann zeta functions may be evaluated from

$$\zeta(2n) = \frac{(2\pi)^{2n}}{2(2n)!}|B_{2n}|, \tag{A6}$$

where the B_{2n} are Bernoulli numbers of even order, e.g., $B_2 = 1/6$, $B_4 = 1/30$, $B_6 = 1/42$, $B_8 = 1/30$, and so on. For large n, the approximation $\zeta(n + 2) \approx (\zeta(n) + 3)/4$ is useful.

APPENDIX B: APPROXIMATION TO LOGARITHMIC INTEGRAL

Consider the function defined by

$$U(x) = \int_{-\infty}^{x} \ln(1 + e^y)dy. \tag{B1}$$

The special value $U(0) = \zeta(-2) = \pi^2/12$. Here, convenient approximations are developed which are accurate to within 1% for all x. Consider first arguments of U less than 0, for which the integrand may be Taylor expanded in e^y and integrated term by term. We have

$$U(-x) = \sum_{j=1}^{\infty}\frac{(-1)^{j-1}}{j^2}\exp(-jx). \tag{B2}$$

Let $U(x < 0)$ be parametrically approximated by $U(x) \approx e^x[1 - be^{ax}]$, where a and b are determined from Eq. (B2) and its first derivative evaluated at $x = 0$. It follows that a and b so defined are

$$a = 12\left(\frac{\pi^2 - 12\ln(2)}{12 - \pi^2}\right), \qquad b = 1 - \frac{\pi^2}{12}, \tag{B3}$$

and are numerically equal to $a = 0.728\,43$ and $b = 0.177\,53$. From the definition of $U(x)$, it follows that

$$U(x) = \frac{1}{2}x^2 + 2U(0) - U(-x). \tag{B4}$$

The approximation for $U(x)$, accurate to better than 1% for all x, is then

$$U(x) = \begin{cases} e^x(1 - be^{ax}) & x \leq 0, \\ \left[\frac{1}{2}x^2 + \frac{1}{6}\pi^2 - e^{-x}(1 - be^{-ax})\right] & x > 0. \end{cases} \tag{B5}$$

Equation (B5) is analogous to the "Fowler function" [Eq. (9) of Ref. [34]] and is more amenable to numerical work than forms given by either Fowler or DuBridge.

[1] P. G. O'Shea and H. P. Freund, Science **292**, 1853 (2001).
[2] W. E. Spicer and A. Herrera-Gómez, SLAC-PUB-6303, 1993, SLAC/SSRL-0042, 1993.
[3] P. Michelato, Nucl. Instrum. Methods Phys. Res., Sect. A **393**, 455 (1997).
[4] J. A. Nation, L. Schächter, F. M. Mako, L. K. Len, W. Peter, C.-M. Tang, and T. Srinivasan-Rao, Proc. IEEE **87**, 865 (1999).
[5] X. J. Wang, T. Srinivasan-Rao, K. Batchelor, I. Ben-Zvi, and J. Fisher, Nucl. Instrum. Methods Phys. Res., Sect. A **356**, 159 (1995).
[6] D. W. Feldman, M. Virgo, P. G. O'Shea, and K. L. Jensen, in *Proceedings of the 24th International Free Electron Laser Conference, Argonne, IL, 2002* (IEEE, Piscataway, NJ, 2002).
[7] K. L. Jensen, Y. Y. Lau, and B. Levush, IEEE Trans. Plasma Sci. **28**, 772 (2000).
[8] C. R. K. Marrian and A. Shih, IEEE Trans. Electron Devices **36**, 173 (1989).
[9] R. Thomas, Naval Research Laboratory (unpublished) (data obtained from A. Shih and J. Yater).

[10] K. L. Jensen, D.W. Feldman, M. Virgo, and P. G. O'Shea (to be published).
[11] E. M. Logothetis and P. L. Hartman, Phys. Rev. **187**, 460 (1969).
[12] R. Yen, J. M. Liu, N. Bloembergen, T. K. Yee, J. G. Fujimoto, and M. M. Salour, Appl. Phys. Lett. **40**, 185 (1982).
[13] H. E. Elsayed-Ali, T. Juhasz, G. O. Smith, and W. E. Bron, Phys. Rev. B **43**, 4488 (1991).
[14] T. Tsang, Appl. Phys. Lett. **63**, 871 (1993).
[15] D. M. Riffe, X. Y. Wang, M. C. Downer, D. L. Fisher, and J. L. Erskine, J. Opt. Soc. Am. B **10**, 1424 (1993).
[16] B. Leblond, G. Kuznetsov, and M. Batazova, Nucl. Instrum. Methods Phys. Res., Sect. A **372**, 562 (1996).
[17] N. A. Papadogiannis, S. D. Moustaïzis, and J. P. Girardeau-Montaut, J. Phys. D **30**, 2389 (1997); N. A. Papadogiannis and S. D. Moustaïzis, J. Phys. D **34**, 499 (2001).
[18] C. Hernandez-Garcia and C. A. Brau, Nucl. Instrum. Methods Phys. Res., Sect. A **483**, 273 (2002).
[19] R. E. Thomas, J.W. Gibson, G. A. Haas, and R. H. Abrams, Jr., IEEE Trans. Electron Devices **37**, 850 (1990).
[20] G. Gärtner, P. Geittner, D. Raasch, and D. U. Wiechert, Appl. Surf. Sci. **146**, 22 (1999).
[21] A. Shih, J. E. Yater, and R. Abrams, Appl. Surf. Sci. **146**, 1 (1999).
[22] H. Ibach and H. Lüth, *Solid State Physics* (Springer-Verlag, Berlin, 1996), 2nd ed.
[23] C. Kittel, *Introduction to Solid State Physics* (Wiley, New York, 1976), 2nd ed.
[24] George T. Furukawa and Thomas B. Douglas, in *American Institute of Physics Handbook*, edited by Dwight E. Gray (McGraw-Hill, New York, 1972), 3rd ed., Chap. 4e, pp. 4–116.
[25] K. L. Jensen, in *Vacuum Microelectronics*, edited by W. Zhu (Wiley Interscience, New York, 2001), Chap. 3.
[26] K. L. Jensen, P. G. O'Shea, and D.W. Feldman, Appl. Phys. Lett. **81**, 3867 (2002).
[27] L. E. DuBridge, Phys. Rev. **43**, 727 (1933).
[28] C. Herring and M. H. Nichols, Rev. Mod. Phys. **21**, 187 (1949).
[29] K. L. Jensen, J. Vac. Sci. Technol. B (to be published).
[30] Spectra-Mat, Inc., 100 West Gate Drive, Watsonville, CA 95076, USA, http://www.spectramat.com
[31] V. S. Fomenko, in *Handbook of Thermionic Properties - Electronic Work Functions and Richardson Constants of Elements and Compounds*, edited by G.V. Samsonov (Plenum Press Data Division, New York, 1966).
[32] I. S. Gradshteyn and I. M. Ryzhik, *Table of Integrals, Series, and Products* (Academic Press, New York, 1981).
[33] E.V. Haynsworth, in *Handbook of Mathematical Functions*, edited by M. Abromowitz *et al.* (Dover, New York, 1972).
[34] R. H. Fowler, Phys. Rev. **38**, 45 (1931).